

VU Research Portal

Structural and spectroscopic in vivo imaging of the human retina with scanning light ophthalmoscopy

Damodaran, M.

2020

document version

Publisher's PDF, also known as Version of record

[Link to publication in VU Research Portal](#)

citation for published version (APA)

Damodaran, M. (2020). *Structural and spectroscopic in vivo imaging of the human retina with scanning light ophthalmoscopy*. [PhD-Thesis - Research and graduation internal, Vrije Universiteit Amsterdam].

General rights

Copyright and moral rights for the publications made accessible in the public portal are retained by the authors and/or other copyright owners and it is a condition of accessing publications that users recognise and abide by the legal requirements associated with these rights.

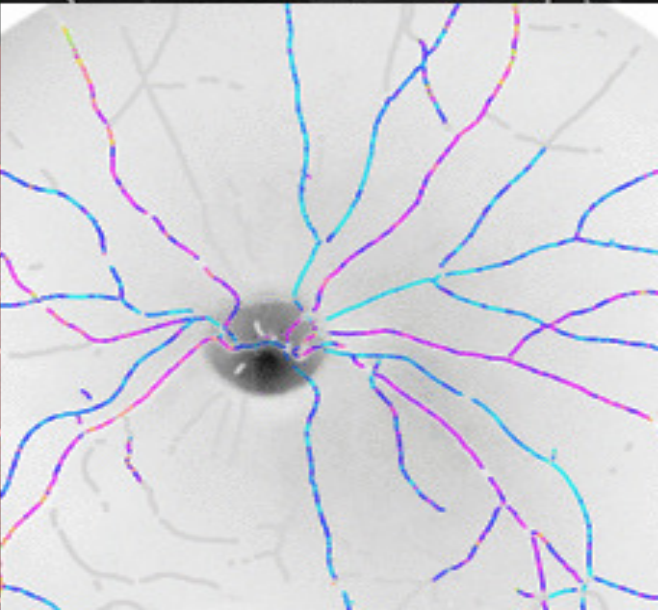
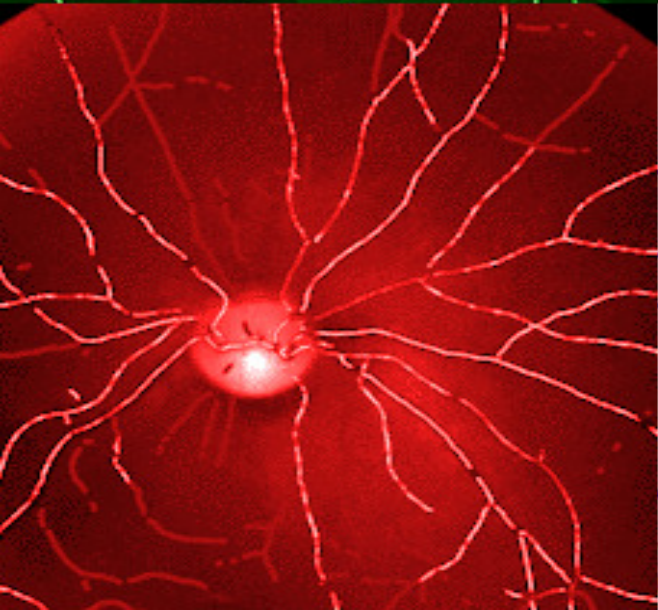
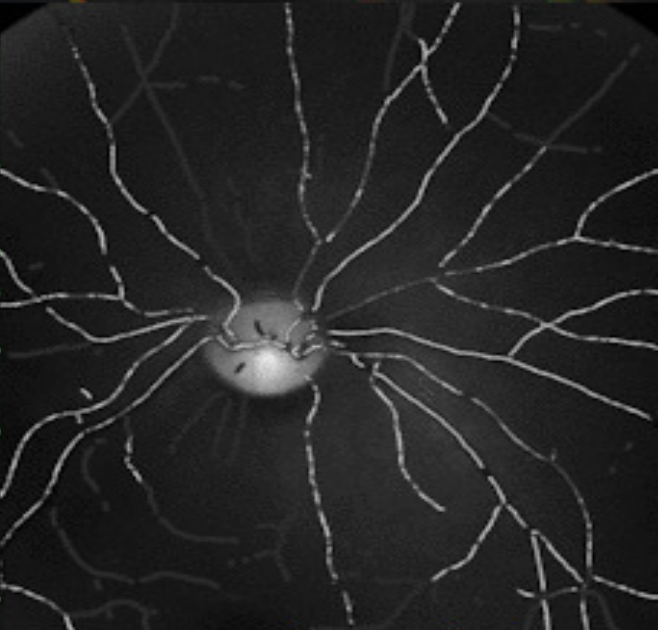
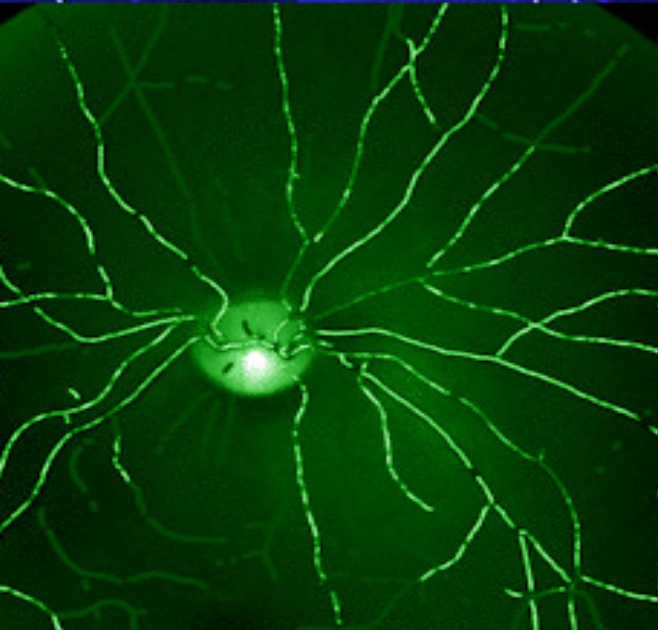
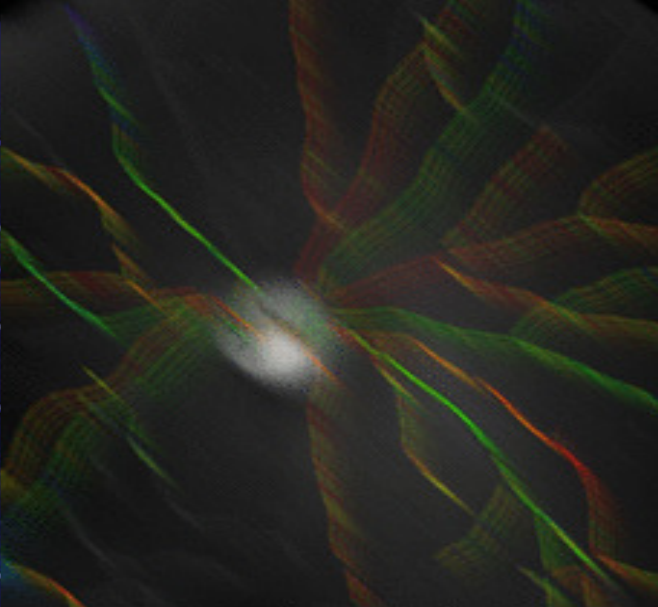
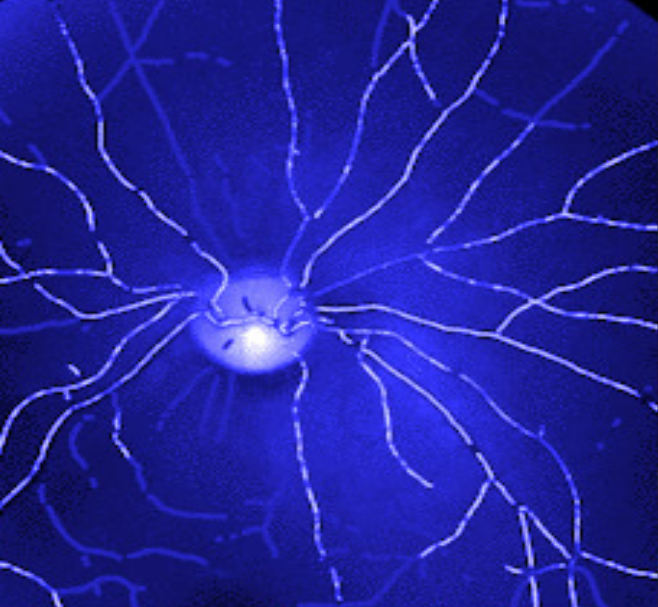
- Users may download and print one copy of any publication from the public portal for the purpose of private study or research.
- You may not further distribute the material or use it for any profit-making activity or commercial gain
- You may freely distribute the URL identifying the publication in the public portal

Take down policy

If you believe that this document breaches copyright please contact us providing details, and we will remove access to the work immediately and investigate your claim.

E-mail address:

vuresearchportal.ub@vu.nl



5

sub-diffuse scanning laser oximetry of the human retina *in vivo*

5

based on :

M. Damodaran, A. Amelink, F. Feroldi, B. Lochocki, V. Davidoiu, and J. F. de Boer,
"In vivo subdiffuse scanning laser oximetry of the human retina the human retina,"
J. Biomed. Opt. **24**, (2019).

Abstract

Scanning laser ophthalmoscopes (SLOs) have the potential to perform high speed, high contrast, functional imaging of the human retina for diagnosis and follow up of retinal diseases. Commercial SLOs typically use a monochromatic laser source or a superluminescent diode for imaging. Multispectral SLOs using an array of laser sources for spectral imaging have been demonstrated in research settings, with applications mainly aiming at retinal oxygenation measurements. Previous SLO based oximetry techniques are predominantly based on wavelengths that depended on laser source availability. In this paper, we describe a novel SLO system based on a supercontinuum source and a double-clad fibre using the single mode core for illumination and the larger inner cladding for quasi-confocal detection to increase throughput and signal to noise. A balanced detection scheme was implemented to suppress the relative intensity noise of the supercontinuum source. The SLO produced dual wavelength, high-quality images at 10 frames per second with a maximum 20° imaging field of view with any desired combination of wavelengths in the visible spectrum. We demonstrate SLO-based dual wavelength oximetry in vessels down to 50 microns in diameter. Reproducibility was demonstrated by performing 3 different imaging sessions of the same volunteer, 8 minutes apart. Finally, by performing a wavelength sweep between 485 and 608 nm we determined for our SLO geometry an approximately linear relationship between the effective path length of photons through the blood vessels and the vessel diameter.

5.1 Introduction

Measuring the amount of oxygenated and deoxygenated haemoglobin present in the retinal vessels is potentially very valuable to detect and monitor retinal diseases. Oxygen saturation in the retinal vasculature is an important indicator of retinal health [1, 2]. Several studies have investigated and found associations between retinal pathologies and retinal vessel oxygen saturation [3–9]. Moreover, retinal vessel oxygen saturation has also been linked to neurodegenerative diseases [10–12]. Various imaging techniques have been employed in the past to measure retinal oxygen saturation [13–22], while recently emerging techniques have enabled oximetry to be applied in a variety of *in vivo* applications [23–25]. Nevertheless, the vast majority of retinal oximetry studies use a fundus camera-based approach, which has a limited spatial resolution and provide insufficient contrast to performing oximetry in retinal microvessels smaller than ~ 100 microns. However, it is in the smaller microvessels that the oxygen saturation is expected to decrease in re-

sponse to local increased metabolic demand or decreased oxygen delivery capacity. The larger retinal vessels that can be resolved by fundus cameras are expected to be much less sensitive to local changes in tissue metabolic demand or microvascular dysfunction; therefore, the microvasculature provides the most clinically relevant information on local tissue metabolic status. This motivates the development of an SLO-based oximeter, capable of resolving the oxygen saturation in vessels as small as ~ 50 micrometres.

We have recently shown that the signal to noise ratio (SNR) of the retinal image strongly influences the accuracy of retinal oximetry [26]. Since the permissible light exposure of the retina is limited in order to prevent injury, it is important to use the allowable light budget efficiently. This implies that imaging should be performed at dedicated wavelength bands, providing the highest SNR for the available light budget. Additionally, averaging of multiple scans of the retina at each wavelength may be necessary to reach a target SNR required to achieve the desired oxygen saturation accuracy.

In this paper, we demonstrate the next-generation SLO-based retinal oximeter with optimised wavelengths and throughput, which can measure retinal oxygenation in vessels down to ~ 50 microns diameter. We will first briefly describe the method to select an optimum wavelength for retinal oximetry by taking into account the error on the measured intensities in the retina, the pigment packing effect, the maximum permissible power that can be used for retinal illumination, and the quantum efficiency of the detector. Then we describe the design of an SLO that employs a supercontinuum (SC) source for producing continuous, high contrast images at any desired wavelength from 484 to 700 nm at a speed of 10 frames/second. Balanced detection was implemented to suppress the relative intensity noise (RIN) of the SC source, required to achieve a sufficiently high SNR in the retinal images. Finally, to establish the imaging capabilities of the device, healthy volunteers were imaged. We demonstrate the effect of including an achromatizing lens in the setup to cancel the chromatic aberrations of the eye. Finally, we demonstrate that the extracted oxygen saturation of the smaller retinal vessels is reproducible and within physiological expected ranges.

5.2 Methods

5.2.1 Wavelength selection for dual wavelength retinal oximetry

Oxygenation is typically assessed by imaging the retinal vessels at different wavelengths using multispectral imaging techniques where the choice of wavelengths

will affect the achievable measurement accuracy. In an earlier publication, we provided a detailed explanation and calculation of retinal oximetry with and without the pigment packing effect [26]. Here we present a summary of the calculations but now without assuming the use of an isosbestic wavelength for oximetry, as was done in our previous paper. Furthermore, we will account for the maximum permissible power that can be used for retinal illumination and the quantum efficiency of the detector in the calculations.

Let $I(\bar{x}_b, \lambda)$ and $I(\bar{x}_t, \lambda)$ be the recorded intensities in the retinal image at the centre of the blood vessel and adjacent tissue location, respectively, at a wavelength λ and for equal illumination intensity at both locations. The relative optical density OD_λ of the blood vessel location compared to the surrounding tissue can be written as:

$$OD_\lambda = \ln \left(\frac{I(\bar{x}_t, \lambda)}{I(\bar{x}_b, \lambda)} \right) = \langle L_{eff}(\lambda) \rangle \cdot (S \cdot \mu_a^{HbO_2}(\lambda) + (1 - S) \cdot \mu_a^{Hb}(\lambda)) + G(\lambda) \quad (5.1)$$

where the attenuation of the reflected light due to the blood within \bar{x}_b is governed by *modified Beer-Lamberts law* [27, 28], with $\langle L_{eff}(\lambda) \rangle$, the effective path length of photons travelling through the probed volume before reaching the detector. The absorption coefficients [29] of oxy- and deoxy-haemoglobin are given by $\mu_a^{HbO_2}(\lambda)$ and $\mu_a^{Hb}(\lambda)$, respectively, assuming a concentration of haemoglobin of 15 g/dL. $G(\lambda)$ is a factor which accounts for any apparent increase or decrease in the ODs purely due to scattering differences within the volumes \bar{x}_b and \bar{x}_t . We define the ratio of ODs at 2 wavelengths λ_1 and λ_2 as:

$$\rho_{\lambda_1|\lambda_2} = \frac{OD_{\lambda_1}}{OD_{\lambda_2}} \quad (5.2)$$

We can then write the saturation (i.e., the fraction of the oxygenated haemoglobin concentration to the total concentration of haemoglobin) as [26],

$$S_{\lambda_1|\lambda_2} = \frac{\rho_{\lambda_1|\lambda_2} \cdot \mu_a^{Hb}(\lambda_2) - \mu_a^{Hb}(\lambda_1)}{(\mu_a^{Hb}(\lambda_2) - \mu_a^{HbO_2}(\lambda_2)) \cdot \rho_{\lambda_1|\lambda_2} + (\mu_a^{HbO_2}(\lambda_1) - \mu_a^{Hb}(\lambda_1))} + \alpha \cdot G \quad (5.3)$$

where the factor $\alpha \cdot G$ is an offset, if any, to the saturation due to scattering. The error on the saturation, ΔS is given by,

$$^1\alpha = \frac{\rho - 1}{\langle L_{eff} \rangle \cdot \nu \cdot ((\mu_a^{HbO_2}(\lambda_2) - (\mu_a^{Hb}(\lambda_2)) \cdot \rho) + (\mu_a^{HbO_2}(\lambda_1) - (\mu_a^{Hb}(\lambda_1)))}$$

$$\Delta S = \frac{dS}{d\rho} \cdot \Delta\rho \quad (5.4)$$

where the error in $\rho_{\lambda_1|\lambda_2}$, $\Delta\rho$ is given by the underlying error in the ODs resulting from the error in recorded intensities (please refer to Damodaran *et al.*[26] for mathematical expressions relating ΔS to ΔI). The error in saturation can be calculated using Eq. 6.4. The result is plotted in Fig. 5.1 for different wavelength combinations where $\lambda \in [460 \text{ } 650] \text{ nm}$ and the standard error on the mean recorded intensity values ($\Delta I/I$) was assumed to be 1%. This figure shows the wavelength combinations that give the smallest saturation errors for a given saturation level. Fig. 5.1 depends on Eq. 6.3, which is correct for a large blood vessel present superficially in the retina with a diameter comparable to the collection area. In case of a small blood vessel embedded in the scattering retinal tissue that is illuminated with a narrow beam, and when the collection aperture is much larger than the illumination aperture and the blood vessel diameter, then the blood vessel occupies only a small portion of the total probed volume and hence the pigment packing effect should be considered and incorporated into the ODs [26, 30, 31]. Equation 6.3 can then be written as,

$$S_{\lambda_1|\lambda_2,pp} = \frac{\rho_{\lambda_1|\lambda_2} \cdot \frac{C_{\lambda_2}}{C_{\lambda_1}} \cdot \mu_a^{Hb}(\lambda_2) - \mu_a^{Hb}(\lambda_1)}{(\mu_a^{Hb}(\lambda_2) - \mu_a^{HbO_2}(\lambda_2)) \cdot \rho_{\lambda_1|\lambda_2} \cdot \frac{C_{\lambda_2}}{C_{\lambda_1}} + (\mu_a^{HbO_2}(\lambda_1) - \mu_a^{Hb}(\lambda_1))} + \alpha \cdot G \quad (5.5)$$

where C_λ is the correction factor to include the pigment packing effect and $\alpha \cdot G^2$ is an offset due to scattering. It can be observed that if the ratio of correction factors $C_{\lambda_2}/C_{\lambda_1}$ in Eq. 5.5 is 1, Eq. 5.5 reduces to Eq. 6.3 i.e., $C_{\lambda_2}/C_{\lambda_1} \simeq 1 \Rightarrow S_{\lambda_1|\lambda_2} \simeq S_{\lambda_1|\lambda_2,pp}$.

Figure 5.2A shows an ensemble ΔS where weights of 0.4, 0.6, 0.8, 1.0 and 1.0 were applied to the five different saturation graphs $S = 0.00, 0.25, 0.50, 0.75$ and 1.00 in Fig. 5.1, respectively. The weights were chosen to favour the more physiologically relevant, health range of oxygen saturation [32]. Figure 5.2B shows the difference in calculated saturation with and without the pigment packing effect defined as the saturation offset, S_{offset} ($S_{offset} = S_{\lambda_1|\lambda_2} - S_{\lambda_1|\lambda_2,pp}$) due to the pigment packing effect when the same weights were applied. Figure 5.2C shows addition of the saturation offset and the saturation error for wavelengths $\lambda_1, \lambda_2 \in [450 \text{ } 650]$ respectively. Finally Fig. 5.2D shows Fig. 5.2C corrected for the wavelength dependent maximum permissible exposure (MPE) prescribed for 30000 seconds of

$$^2\alpha = \frac{\rho - 1}{(L_{eff}) \cdot \nu \cdot ((\mu_a^{HbO_2}(\lambda_2) - (\mu_a^{Hb}(\lambda_2)) \cdot \rho \cdot C_{\lambda_2} + (\mu_a^{HbO_2}(\lambda_1) - (\mu_a^{Hb}(\lambda_1)) \cdot \lambda_1))$$

continuous single point exposure[33] (see Fig.15 in Appendix), and responsivity of the detector across the wavelengths[34]. The $\Delta I/I$ value was 1% for the MPE and responsivity at 600 nm, and increases linearly for decreasing MPE and responsivity as a function of wavelength to get Fig. 5.2D. For example at 460 nm, the MPE normalised on the MPE for $\lambda \geq 500$ nm was 0.1 and the responsivity normalised on the responsivity at 600 nm was 0.7 and hence the $\Delta I/I$ was adjusted to 14.3%. Based on Fig. 5.2D, 498 nm and 594 nm wavelengths were chosen for oximetry estimation. Further, this wavelength choice was used as a software setting for central wavelength in the wavelength settings tunable filter of the supercontinuum source. The resulting light spectrum measured with these wavelength settings was convolved with the absorption spectrum values [29] and the following values of the absorption coefficients were obtained and used for calculating the oxygen saturation in the retina : $\mu_a^{Hb}(\lambda_1) = 11.0$, $\mu_a^{HbO_2}(\lambda_1) = 9.5$, $\mu_a^{Hb}(\lambda_2) = 7.3$ and $\mu_a^{HbO_2}(\lambda_2) = 13.1$.

5.2.2 System design

The scanning laser oximeter setup was an adaptation of our previous design [26], with the aim to optimise the SNR of our imaging system. A schematic layout of the system is shown in Fig. 5.3. The light from an SC source (EXU-6, NKT Photonics A/S, Birkerød, Denmark) was filtered using a tunable filter (Select, NKT Photonics A/S, Birkerød, Denmark). A 90:10 fused single-mode 460-HP fibre coupler (TW560R2A2, Thorlabs GmbH, Germany) was used to send 10 % of the light into detection module II for continuous laser power monitoring and balanced detection (see section 2.3). The core of the double clad fibre (DCF) in port S of the DCFC [35, 36] was excited using the 90 % port of the splitter. About 94 % (transmission measured at 550 nm) of this light reached the port A of the DCFC. A reflective fibre collimator (RC02APC-P01, Thorlabs GmbH, Germany) was used to collimate the fibre output from port A into a 2.2 mm beam. This beam size was optimum for two reasons: (i) The beam size was small enough that the beam is not clipped in the pupil of the subject even with the expected pupil constriction due to bright visible radiation. (ii) This beam size was close to the optimum pupil size for lateral resolution [37] A dichroic mirror (D3, long pass cut off 700 nm) was used to prevent any residual pump light of the SC from entering the rest of the system. A custom made dispersion compensating lens (DCL) (Shanghai optics Inc., H-FK61 and K4A, $f = 1800$ mm) was placed in the common beam path to compensate for the longitudinal focal shift arising from the chromatic aberration of the human eye [38]. A combination of a 2.56 kHz resonant scanner (5.12 kHz line rate by utilising both sides of scanner sweep) (EPOC., Glendale, New York, USA), and a 10 Hz galvanometer

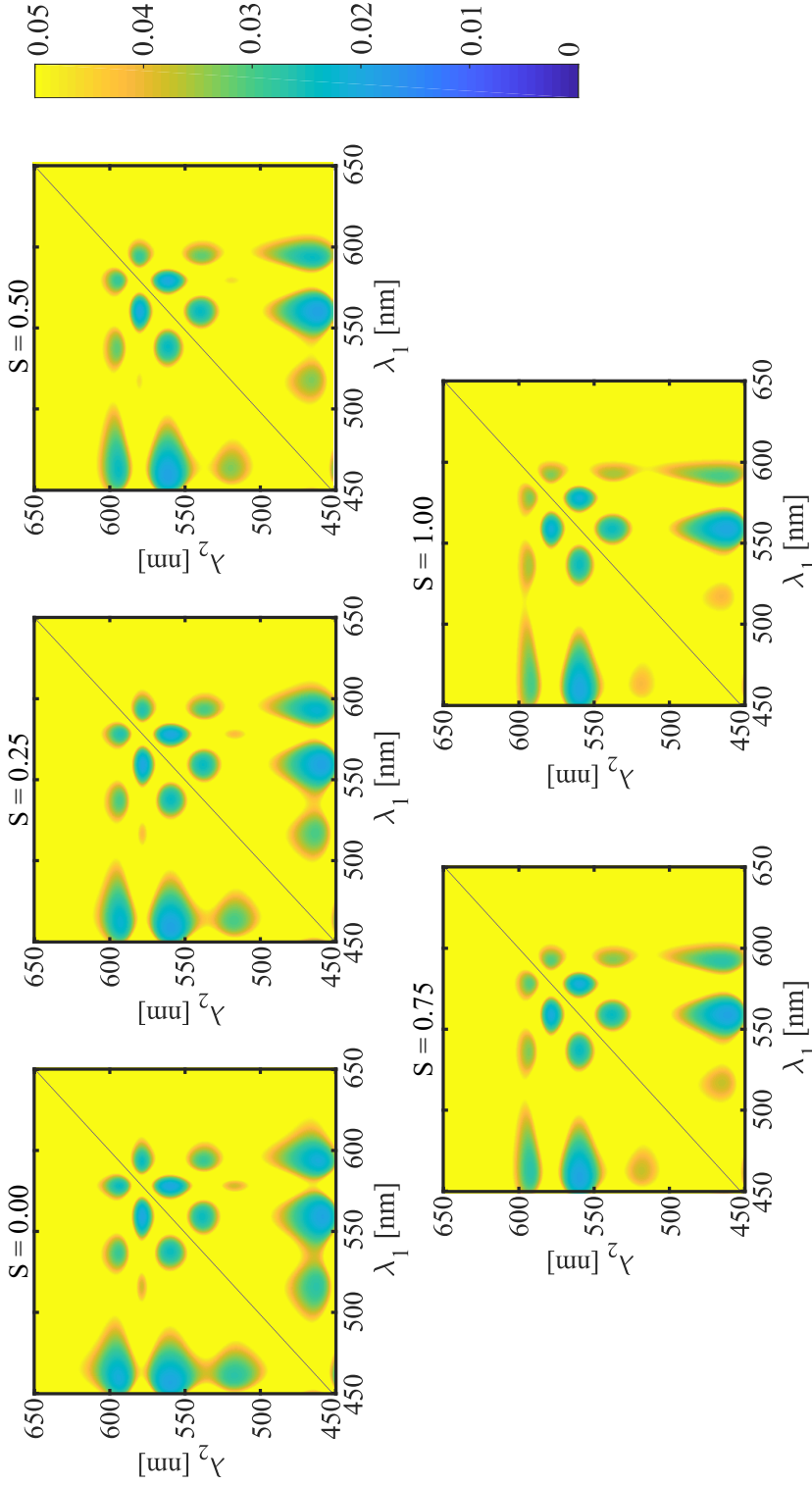


Figure 5.1: *in silico* analysis of saturation error ΔS for different saturation levels and wavelength combinations for $\lambda_1, \lambda_2 \in [450 \text{ } 650]$ nm. The standard error on the mean recorded intensity values ($\Delta I/I$) was assumed to be 1%. All values of $\Delta S > 0.05$ were set to 0.05.

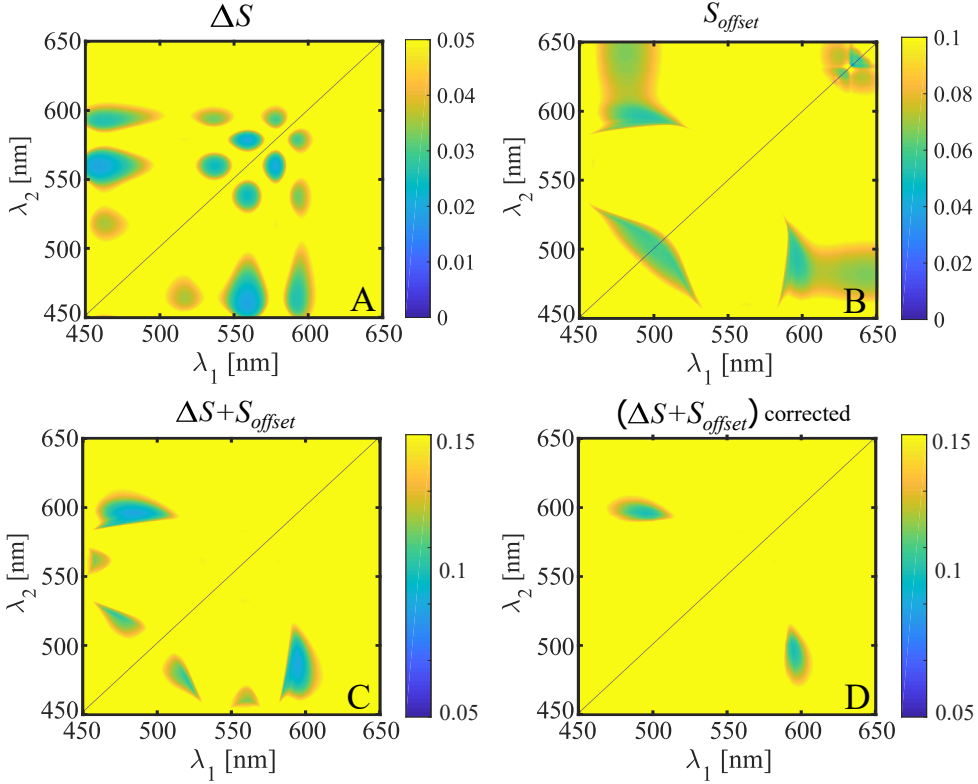


Figure 5.2: *in silico* analysis of saturation error and saturation offset — A: Saturation error ΔS for different wavelength combinations for $\lambda_1, \lambda_2 \in [450 \text{ } 650]$ nm. The standard error on the mean recorded intensity values ($\Delta I/I$) was assumed to be 1%. All values of $\Delta S > 0.05$ are shown as 0.05. B: Calculated saturation difference with and without pigment packing effect shown as an offset ($S_{offset} = S_{\lambda_1|\lambda_2} - S_{\lambda_1|\lambda_2,pp}$) for a 50 μm diameter blood vessel. Values of $S_{offset} > 0.1$ are shown as 0.1. C: Addition of the saturation offset and the saturation error for different wavelength combinations. The color bar has a range [0.05 0.15]. D: Addition of saturation offset and saturation error corrected for the maximum permissible exposure (MPE) prescribed for 30000 seconds of continuous single point exposure (see Appendix), and quantum efficiency of the detector across the wavelengths.

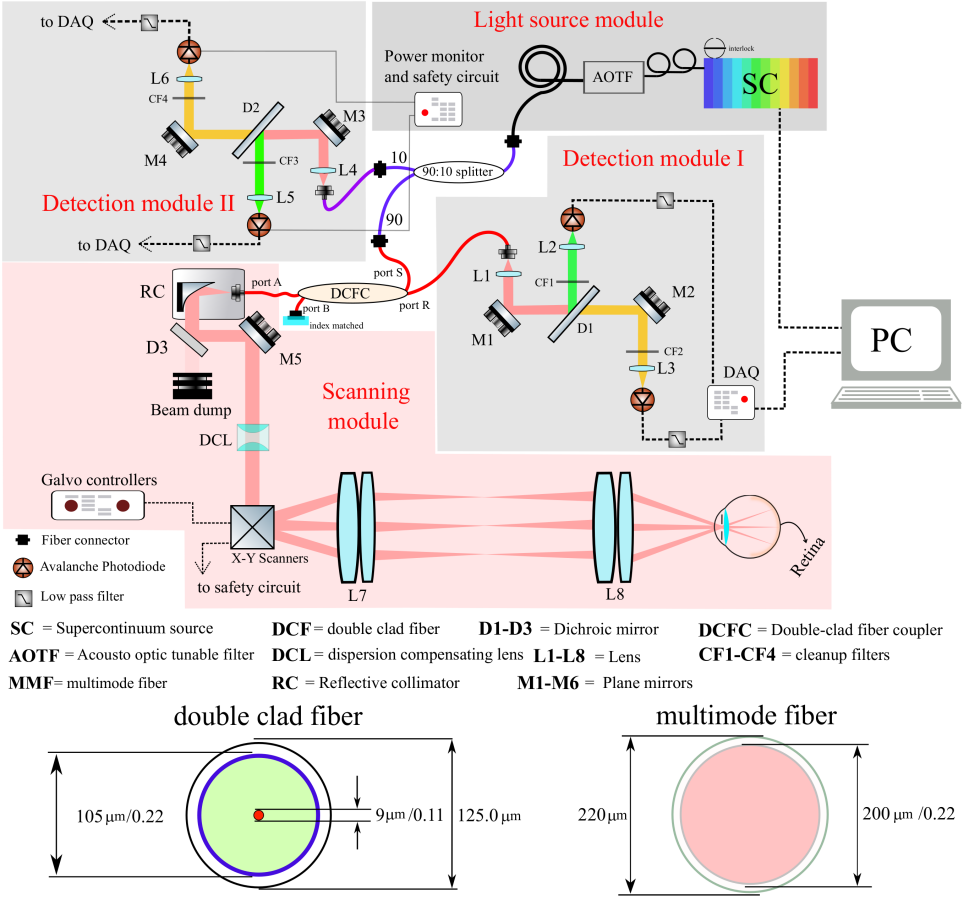


Figure 5.3: A: Schematic sketch of the scanning laser oximeter showing the various components: The abbreviated components are described in the legend. The light from port A of the DCFC was collimated using RC into a 2.2 mm beam. The reflected signal from the retina was collected using the cladding of the DCF with a diameter of 105 μm and a numerical aperture (NA) of 0.22. This light is coupled on to the MMF with a diameter of 200 μm and an NA of 0.22. Thus, the illumination pinhole size is 9 μm and the detection pinhole size is 105 μm . The maximum collection beam diameter of RC was 8 mm. However, the limiting aperture in the optical setup is the pupil of the subject.

mirror (Cambridge tech., Bredford, USA) placed close to each other were used to achieve an imaging throughput of 5.12 million pixels / second (10 frames / second \times 512 lines / frame \times 1000 pixels / line). A 1:1 telescope consisting of achromatic doublet pairs was used to relay a point approximately in the middle of the two scanning mirrors onto the pupil of the eye. The reflected and scattered light from the retina was then collected using the inner cladding of the double clad fibre in port A. About 63 % (transmission measured at 550 nm) of the collected light is then coupled into the multi-mode fibre (MMF). The fibre cross-section of the DCF and the MMF in the DCF coupler are also shown in Fig. 5.3.

The detection modules consist of a collimating lens (L1 and L4, $f = 18$ mm), a dichroic mirror (D1 and D2, long pass cutoff 532 nm), two focusing lenses (L2, L3, L5 and L6, $f = 25$ mm) focusing the spectrally separated light on the active area of avalanche photodiodes (APD) (APD410A2, Thorlabs GmbH, Germany). Two clean-up filters (CF1, CF3: bandpass 470 ± 50 nm, CF2, CF4: long pass 532 nm) were placed just before the focusing lenses to avoid any contribution of light from an unintended wavelength. The detectors in both the detection modules were connected to a 12-bit digitizer (NI-PCI6115, 10 million samples /second /channel, National Instruments, Austin, Texas). The signals from the four detection modules were sampled using four parallel channels of this digitizer running on a single clock. Port B of the DCF coupler was placed in a medium whose index was matching the core index of the MMF to suppress the back reflection from the exit surface of the fibre facet from entering the detection module I.

5.2.3 Balanced detection to increase the signal-to-noise ratio

Spectrally filtering an SC light source provides an excellent wavelength-flexible alternative to the existing approaches of multispectral imaging. However, in an SC light source such as the EXU-6 used in the setup shown in Fig. 5.3, the generation of a large optical bandwidth through non-linear processes [39, 40] results in high relative intensity noise (RIN) compared to traditional sources such as LEDs, lasers, and superluminescent diodes. The fundamental noise limitation of an SC source is described well by Corwin *et al.* [41]. The pulse-to-pulse intensity variations in the SC source amounts to the RIN. In principle, RIN can be suppressed by averaging more pulses within the integration time of the detector. The EXU-6 has a repetition rate of 78 MHz, and given the short integration times of our SLO, (~ 380 ns) only 30 pulses were averaged within an integration time resulting in a significant RIN component in the total noise figure. The total noise power of the system can be written as,

$$\sigma_I^2 = \sigma_{shot}^2 + \sigma_{thermal}^2 + \sigma_{RIN}^2 + \sigma_{DAQ}^2 \quad (5.6)$$

where σ_{shot}^2 is the signal dependent shot noise power, which is the limiting noise component in an ideal heterodyne system, $\sigma_{thermal}^2$ is the signal independent thermal noise power that is inherent to the photodetector, σ_{DAQ}^2 is the noise due to digitization of the signals, and σ_{RIN}^2 is the excess noise due to the RIN of the SC. The signal to noise ratio (SNR) of the detected signal in the APD can be written as,

$$SNR [dB] = 10 \cdot \log \left[\frac{\mu_I}{\sigma_I} \right] \quad (5.7)$$

where μ_I is the mean of the signal and σ_I is the standard deviation of the signal. The noise performance of the EXU-6 SC light source is shown in Fig. 4. The number of detected photons within an integration time was controlled using a fibre attenuator. The thermal noise was measured in the absence of any incident photons, and gradually the number of photons was increased until the detectors reached 90% saturation. By including a 1 MHz low-pass filter with a very sharp cut-off, high frequency noise is eliminated. At each moment, the mean and variance of the photocurrent measured by the detector was determined, and plotted. Figure 5.4 shows that the unbalanced detection suffers from significant RIN contribution (dashed green and red lines). In our balanced detection scheme, The signals of detection module 1 were divided by the respective reference signals of detection module 2 to yield RIN corrected signals for each wavelength. Since OD was calculated as a ratio of two RIN corrected intensities at the same wavelength at different locations, the actual magnitude of the module 2 signals is divided out, so the OD does not depend on the actual magnitude of the module 2 signals. This method resulted in an additional SNR improvement due to RIN suppression. Around 5 dB improvement in signal to noise ratio (SNR) was achieved by using balanced detection and a 1 MHz low-pass filter. Figure 5.4 shows the improvement in SNR achieved by balanced detection for 500 nm and 600 nm wavelengths (dotted green and red lines).

5.2.4 Wavelength sweep hyperspectral imaging

The acousto-optic tunable filter (Select, NKT Photonics A/S, Birkerød, Denmark) used in the system (Fig. 5.3) allows to perform a wavelength sweep for the desired wavelength ranges between 450 and 650 nm and in desired steps (minimum step size 0.1 nm, maximum sweep speed of 10 wavelengths/s). We performed a wavelength sweep from 485 to 608 nm with the SLO with a step size in wave-

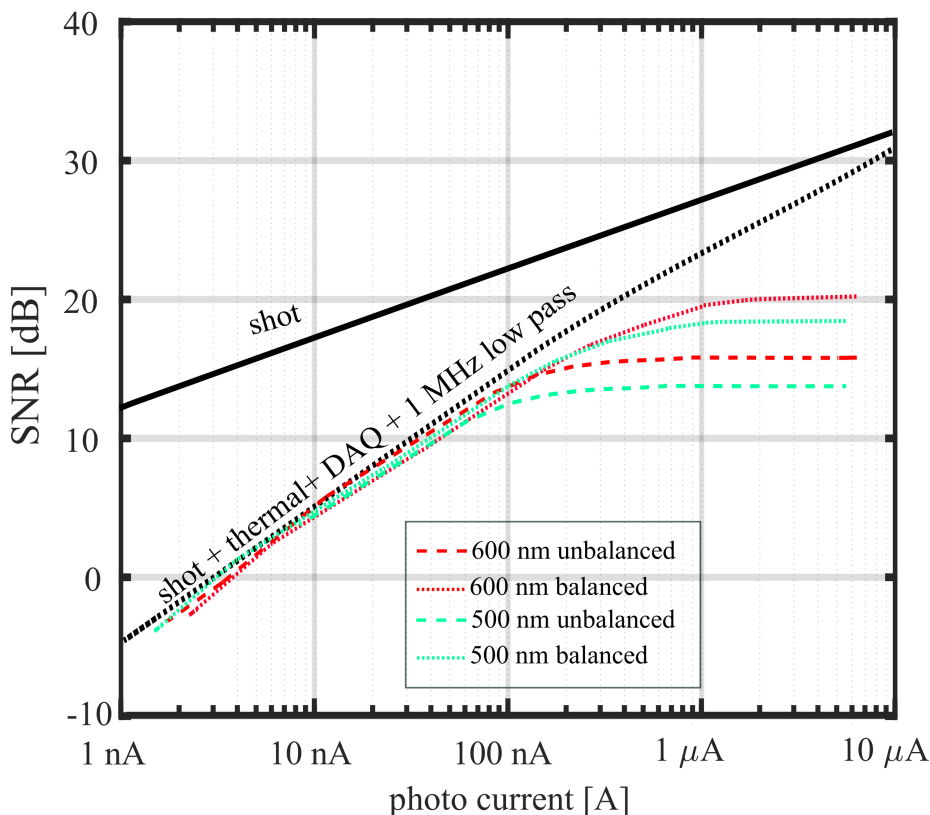


Figure 5.4: Noise performance of the SC source shown by plotting the SNR for different levels of mean signal in the photodetector for two wavelengths, 500nm and 600 nm. The graph shows the theoretical shot noise limited SNR (solid black line), and the expected SNR due to the additional contribution of thermal and quantization noise to the shot noise (dotted black line). The measured SNR for two different wavelengths 500 nm and 600 nm is also shown (dashed green and red line, respectively). The SNR deteriorates for higher photocurrents because RIN noise scales as the square of detected photons in the photodetector. By using balanced detection, an improvement in SNR of approximately 5 dB was achieved for these wavelengths (dotted green and red lines).

length of 3 nm and sweep speed of 1 step/s. Given that the imaging speed of our SLO is 10 fps, this enabled acquiring high-quality retinal images at a rate of 10 images/wavelength within 42 seconds of imaging. For these measurements, the dichroic filters D1, D2 and the clean-up filters CF2 and CF4 (see Fig. 5.3) were removed and only one channel was used in each detection unit.

5.2.5 in vivo human measurements

The clinical pilot study obeyed the principles of the Declaration of Helsinki and was approved for human use by the medical ethical review board at the Amsterdam Universitair Medische Centra (VUmc location), Amsterdam. Tropicamide 0.5 % w./v. drops were administered for pupil dilation during imaging. The optical power used for measuring human subjects was in agreement with the maximum permissible exposure established by the latest IEC standard 60825-1 [33]. The laser safety considerations are detailed in Appendix A. Different FOVs could be implemented by changing the voltages provided to the scanners. Background measurements were taken prior to each imaging session and were subtracted from SLO images to remove artefacts such as lens reflections. In order to utilize the full dynamic range of the detector, strong lens reflections from the last ophthalmic lens in the system were allowed to saturate the detector. All other stray reflections which did not saturate the detector were removed using the background measurements.

5.2.6 Retinal vessel segmentation and oxygenation map

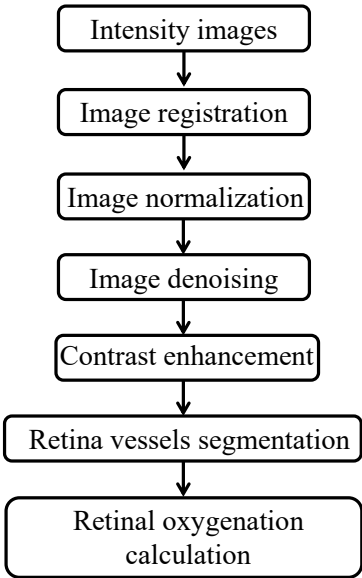


Figure 5.5: Pipeline for vessel segmentation and oxygenation extraction from retinal images.

The SLO images were background corrected by performing a reference measurement before imaging *in vivo*. The background subtracted images were corrected for the sinusoidal scanning of the resonant scanner into a single image. The



retinal oxygenation was constructed using the flow diagram shown in Fig. 5.5. First, several linear intensity images were registered using the scale-invariant feature transform method (SIFT) [42]. After correcting the images for translation, rotation and affine transformations, an averaged image was constructed from the registered data. In order to segment and extract the vessels in the retinal image, the averaged image $Im(x, y)$ was normalized as $Im_N(x, y) = \frac{Im(x, y) - \min[Im(x, y)]}{\max[Im(x, y)] - \min[Im(x, y)]}$, where min and max are defining the minimum and the maximum values in the registered and averaged image. Under the assumption that the SLO images have an approximate piecewise constant structure, the images were denoised using a total variation (TV) algorithm in order to preserve the vessel edges. Subsequently, contrast enhancement was applied to determine the blood vessel boundaries correctly. As has been shown by Davidoiu *et al.* [43], a regularization TV model using a specialized fixed-point algorithm and isotropic total variation (ITV) norm improved the 2D vasculature network segmentation for ex-vivo heart data. In our case, the regularization parameter in the total variation algorithm has been fixed and chosen to be equal to the standard deviation of the normalized image and the convergence stopping parameter value has been set to 0.01. The contrast enhancement of the denoised image was performed using a method called contrast-limited adaptive histogram equalization (CLAHE) [44]. Finally, the blood vessels detection and diameter calculation was performed using wavelets and edge location refinement (ARIA) [45]. The extracted vessel boundary coordinates were exported to Matlab, and were applied to the averaged image $Im(x, y)$. The extraction of the blood and tissue intensity values was done using the method described by Damodaran *et al.* [26].

5.3 Results and discussion

5.3.1 Technical aspects regarding multispectral SLO with an SC source

SNR improvement by balanced detection

Figure 5.6 shows the comparison between *in vivo* retinal images with and without balanced detection in three different volunteers with three different wavelengths. These images clearly show the improvement in image quality due to balanced detection. As described in section 2.3, the RIN of the supercontinuum source was mitigated by using a balanced detection scheme. This resulted in an SNR improvement of 5 dB.

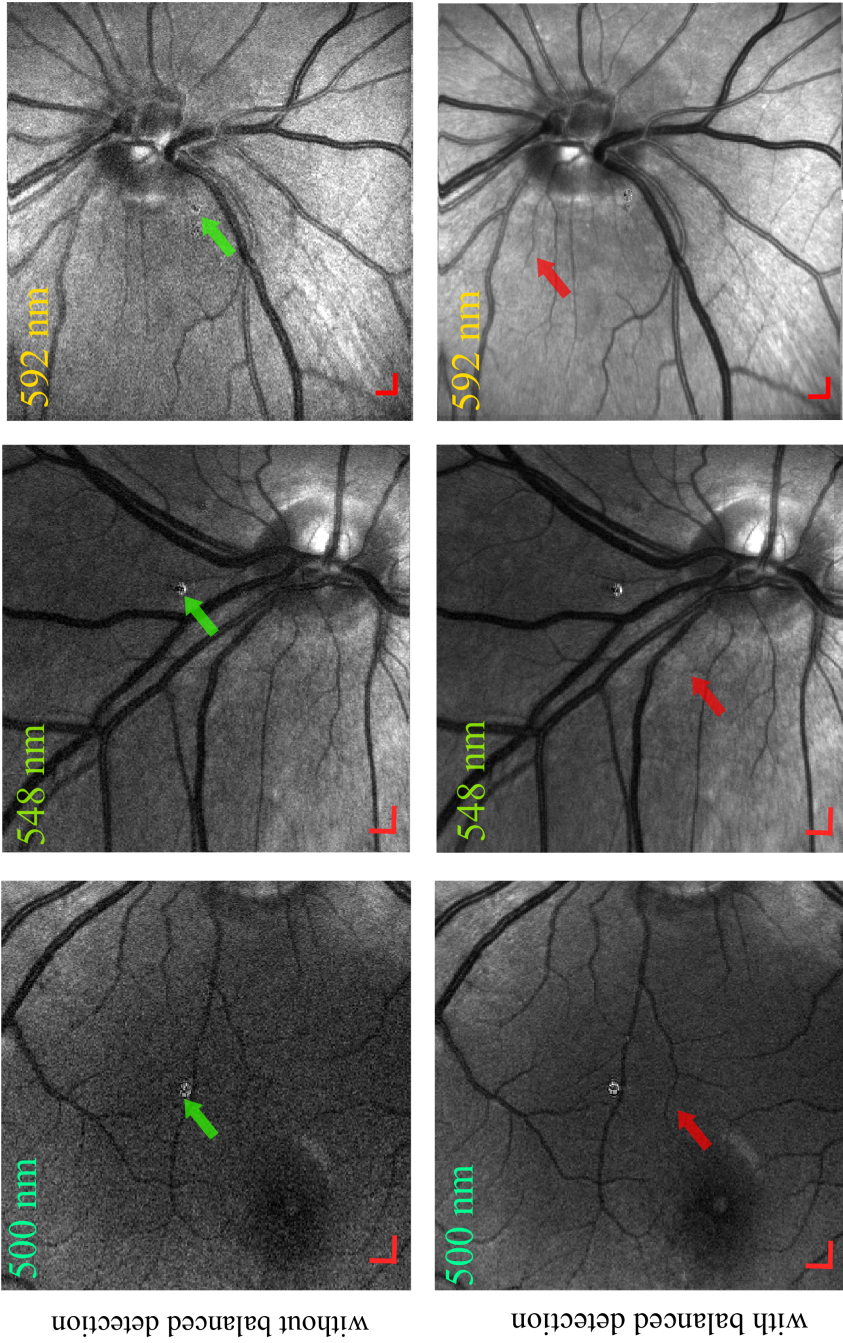


Figure 5.6: Comparison of images with and without balanced detection — unaveraged retinal images from three different volunteers show the improvement in image quality due to balanced detection. The red arrows show the blood vessels that become visible only due to balanced detection. The green arrows point to the lens reflection artefact that saturated the detector, and was not removed due to background subtraction. Scale bar represents 300 μm in the retina.

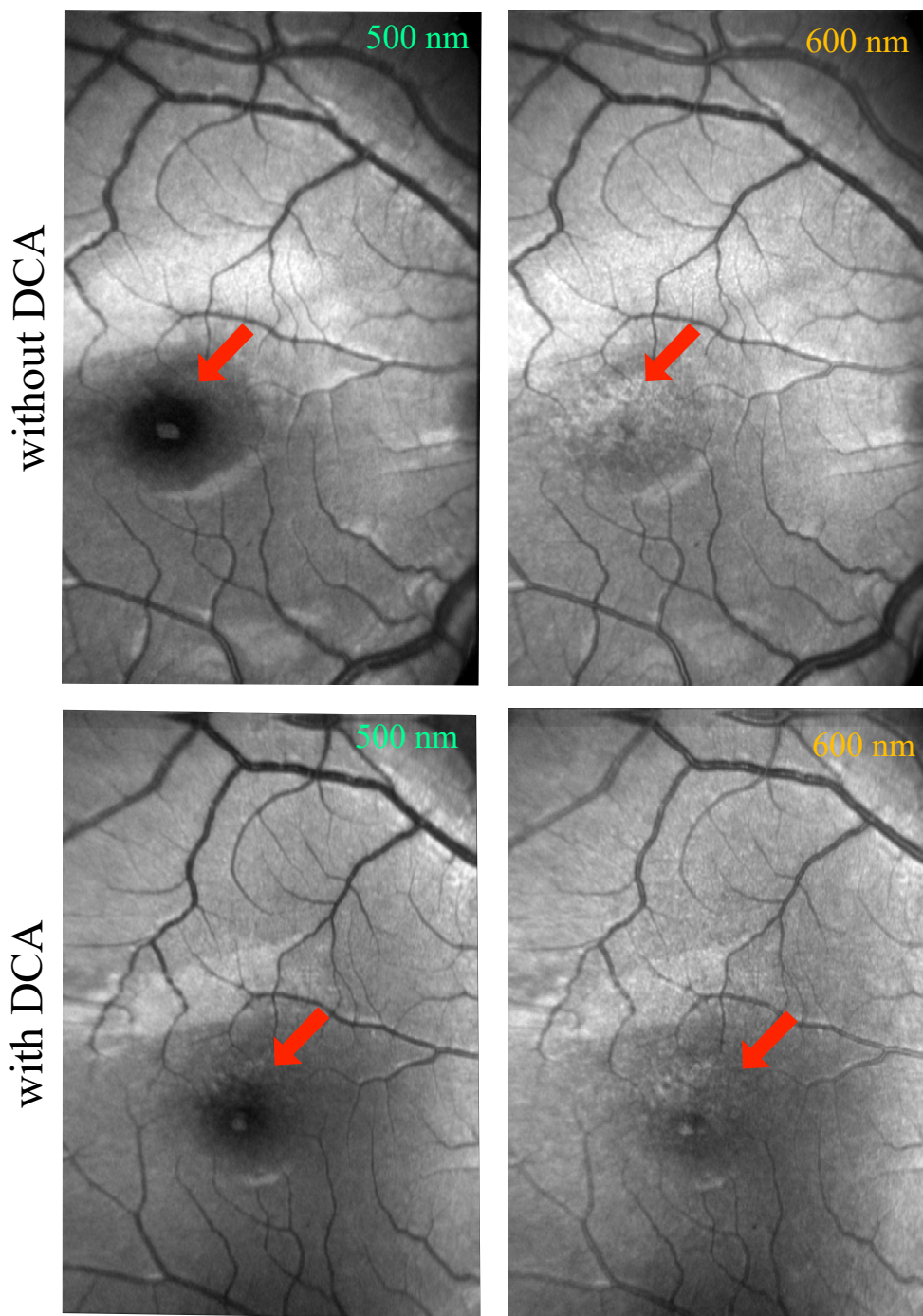


Figure 5.7: Images from right eye of a human volunteer shows the effect of LCA in the absence or presence of a dispersion compensation lens. The foveal pit (red arrows) appear more uniform in the images with dispersion compensation (below) compared to the images without dispersion compensation (top). Scale bar represents 300 μm in the retina.

Compensation for chromatic aberrations of the eye

Chromatic aberrations in the human eye have been studied previously [46, 47]. The longitudinal chromatic aberration (LCA) is a potential source of error in oximetry due to the dispersion in the human eye [38]. LCA causes the spatial location of each pixel in the multispectral image to be in a slightly different axial plane for different wavelengths. This effect can lead up to a 220 μm longitudinal focal shift between the 498 nm and 594 nm wavelengths [48]. This effect can be corrected, as has been shown previously by others [49, 50], by using a dispersion compensating lens in the beam path.

Images acquired at 500 nm and 600 nm without the dispersion compensation lens (Fig. 5.7) in the right eye of a healthy human volunteer demonstrate that chromatic aberrations affect the multiwavelength SLO images; note the difference in the appearance of the foveal pit in the 500 nm and 600 nm images. This can be explained by a focal position that is at the depth of the foveal pit for the 600 nm image, while the 500 nm image has a shallower focus as evidenced by the dark appearance of the foveal pit due to confocal gating. This focal separation between the different wavelengths was compensated by a dispersion compensation lens (Fig. 5.3) that resulted in the images (Fig. 5.7 (bottom)) having a more uniform appearance of the foveal pit between the 500 nm and 600 nm channels. These images are similar to LCA-compensated images published by Larocca *et al.* [50].

The transverse chromatic aberrations (TCA) between the wavelengths was compensated in post-processing of the images by applying a transformation metric which aligns the images of different wavelengths to a chosen wavelength.

Effect of the size of the illumination and collection apertures of the DCF coupler

We determined the effect of using a double clad fibre with different core and inner cladding diameters on throughput and sharpness of the image. Double clad fibre couplers with the same multimode fibres, but different DCFs (different core and inner cladding diameters) were used. Figure 5.8A shows an unaveraged SLO image of right eye of a healthy male volunteer imaged with a DCF having a core diameter of 2.3 μm (single mode at 430 nm) and an inner cladding of 15 μm compared with a DCF having a core diameter of 9 μm and inner cladding diameter of 105 μm (figure 5.8B). The figs show that while the 2.3 μm /15 μm DCF gives images with sharper appearance, this comes at the cost of throughput as indicated by the intensity scale bars. For sub diffuse measurements with higher throughput requirements for fast quantitative imaging, the 9 μm /105 μm DCF is better suited since the amount of averaging required to achieve an SNR of 20 dB is smaller than for the 2.3 μm /15 μm

DCF.

5.3.2 *in vivo* two wavelength oximetry

Retinal oximetry was demonstrated in two healthy volunteers using the optimal two wavelengths, 498 nm and 594 nm. Figure 9A and 9B show the retinal images at 498 nm and 594 nm, respectively. After vessel segmentation and analysis as described section 2.6, an oxygen saturation map of the blood vessels was created and overlaid on the 594 nm image as shown in Fig. 5.14C. Figure 5.14D shows an image taken with the Oxymap Tx for comparison. Similar measurements were made in volunteer 2, as shown in Fig. 5.9. The smallest vessels for which oxygen values are provided are 40 micrometres in diameter.

To analyse the repeatability of the oxygenation measurements, volunteer 1 was imaged three times with 8 minutes intervals in between the measurements. The average oxygenation in 4 vessels (vessel 1-3: arteries; vessel 4: vein) are shown in Fig. 5.10. The calculated oxygenation values in these vessels reproduce very well, despite the difference in positioning of the eye between the 3 imaging sessions, resulting in different overall intensity levels and differences in focus depth, as evidenced by the different appearance of the foveal pit across the 3 sessions.

5.3.3 Wavelength sweep hyperspectral imaging

Similar to other SLO systems, the system described in Fig. 5.3 can image different sections of the retina at high frame rates, but the SC source used in our system also has the advantage of imaging at any desired wavelength and to sweep wavelengths in selected ranges and steps in the 484 to 700 nm range. Figure 5.11 shows the *in vivo* result of a wavelength sweep from 485 to 608 nm performed in Volunteer 2. The measurement took 42 seconds to complete, and each wavelength image shown in the figure was registered to the first frame of that wavelength and averaged in post-processing. As a result of the balanced detection and well-fixated eye of the volunteer, the images exhibit good contrast.

Six blood vessels providing a wide range of vessel diameters were selected from the spectral cube and the OD values were obtained for these vessels after performing the vessel segmentation in individual images. The weighted mean and the standard deviation (weights = $1/\text{standard error}$) were obtained for these vessels and Equation 5.1 (where G was assumed to be 0 and the blood haemoglobin concentration was assumed to be 15 g/dL) was used as the model to perform a weighted fit the OD values in order to extract the $\langle L_{eff} \rangle$ and S values as shown in Fig. 5.12.

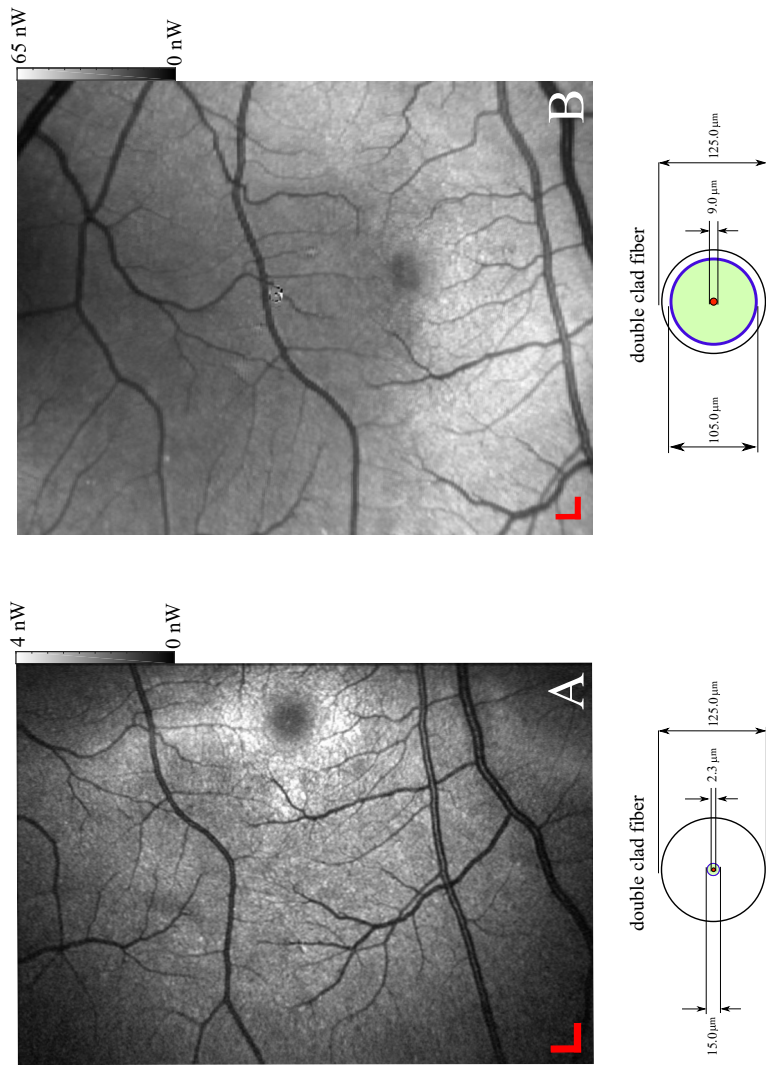


Figure 5.8: Unaveraged retinal SLO images (single frame each) from the described design in section 2.2 with different double clad fibers: A – DCF with a core 2.3 μm diameter and an inner cladding of 15 μm . B — DCF with a core 9 μm diameter and an inner cladding of 105 μm . The cross section of the DCF is shown in the bottom diagrams. Scale bar is 300 μm in the retina.

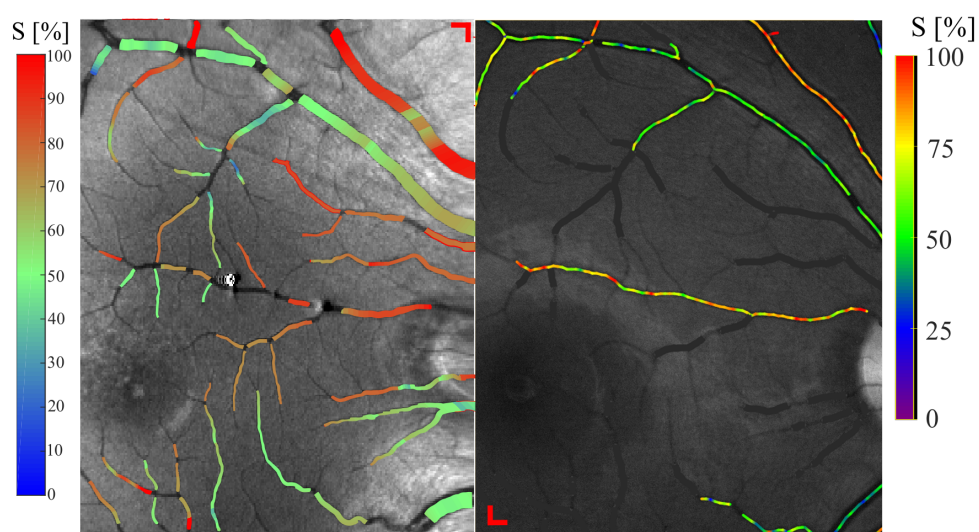


Figure 5.9: A: Estimated oxygenation values in volunteer 2; B: Corresponding image by Oxymap Tx. Scale bar represents 300 μm in the retina.

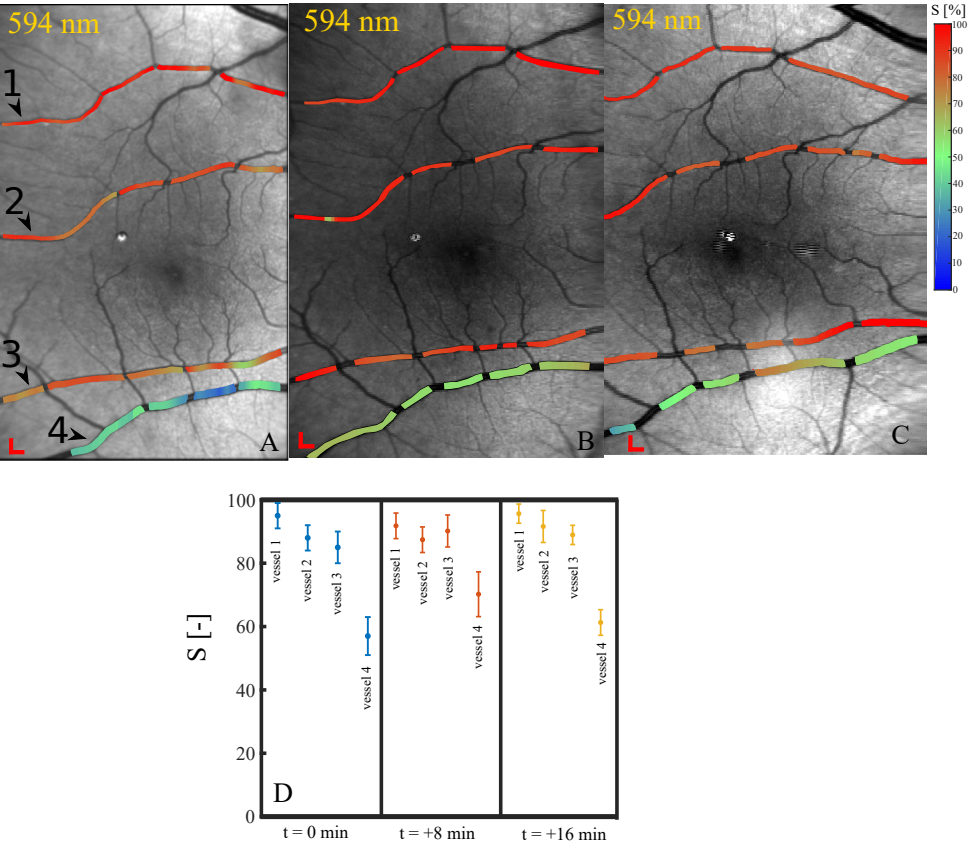


Figure 5.10: Retinal imaging was performed in Volunteer 1 with an interval of 8 minutes to study the repeatability of the measurements. A-C: Measurements made at 0, 8 and 16 minutes in Volunteer 1 with the calculated oximetry for 3 large arteries and a vein. Scale bar represents 300 μm The numerical values are plotted in D.

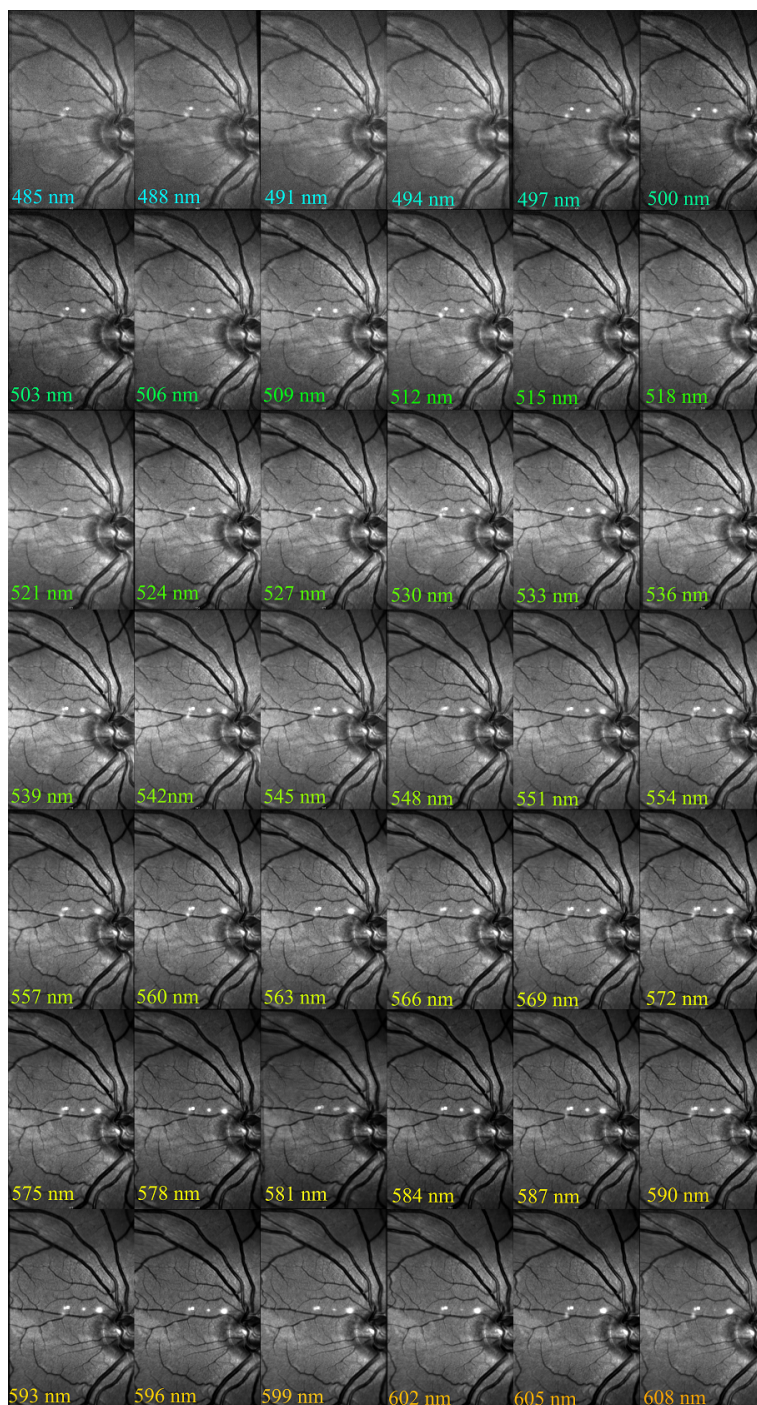


Figure 5.11: Wavelength sweep from 485 nm to 608 nm

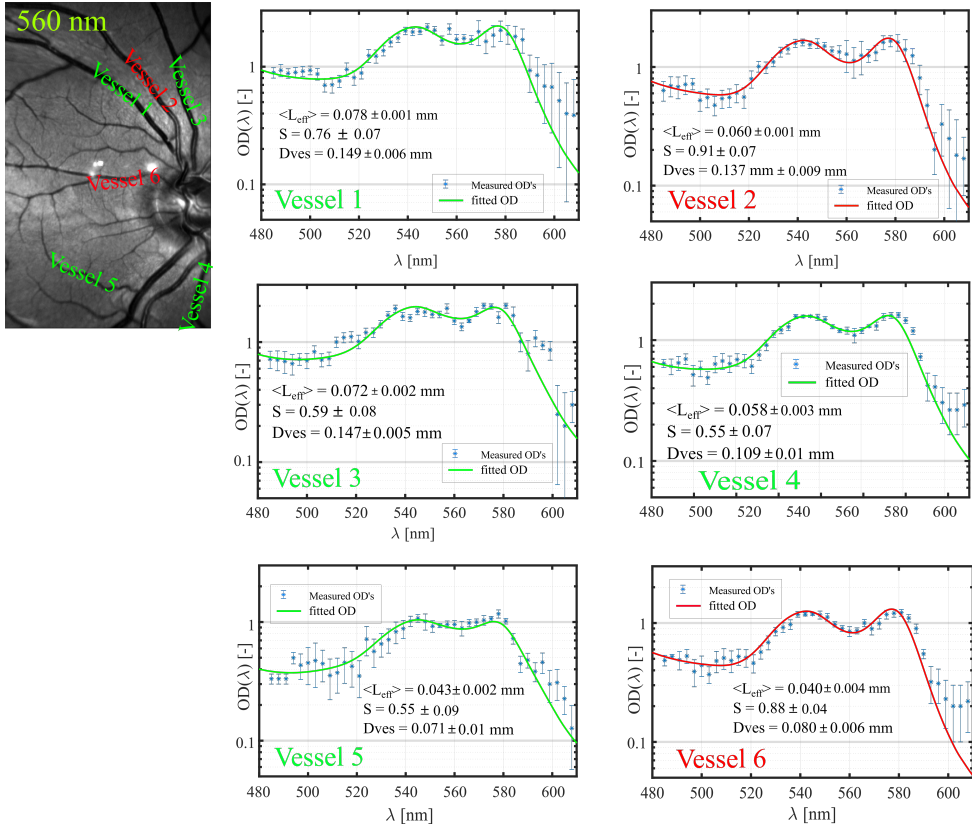


Figure 5.12: Plot of OD as a function of wavelength for six blood vessels in the right eye of a healthy volunteer.

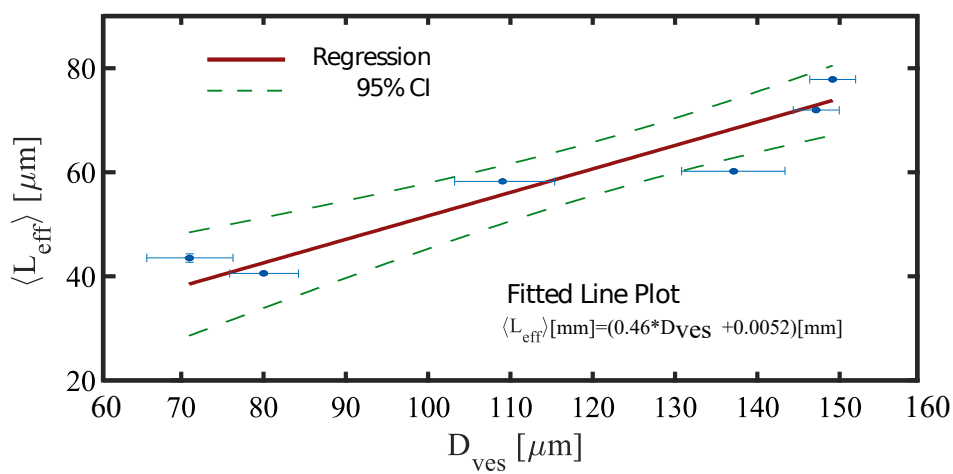


Figure 5.13: Linear regression fit of the effective path length $\langle L_{eff} \rangle$ as a function of the blood vessel diameter D_{ves}

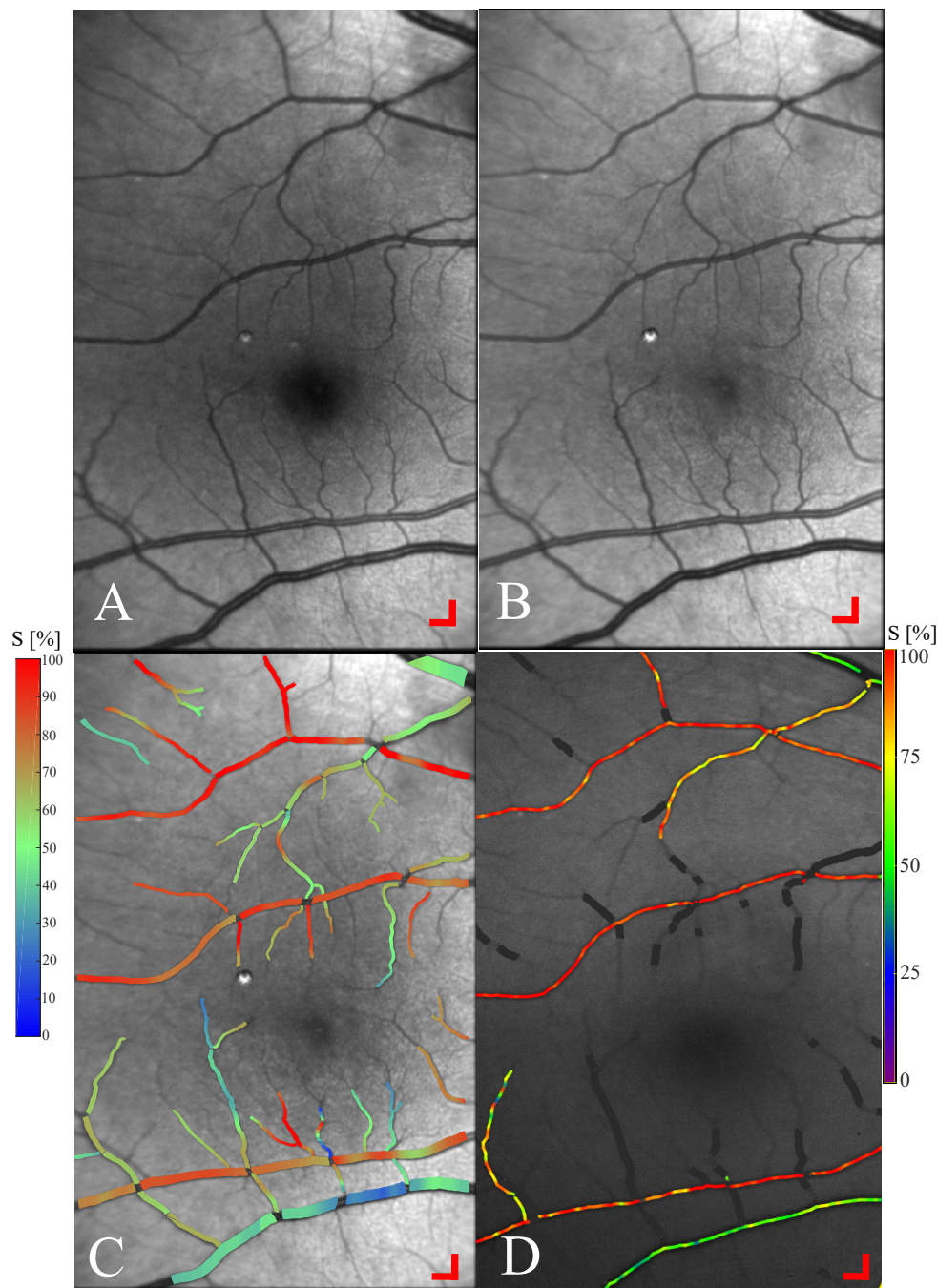


Figure 5.14: SLO images taken from a healthy human volunteer at two wavelengths 498 nm (A) and 594 nm (B). 10 frames were registered and averaged to improve the SNR of the images. The estimated oximetry results are shown in C. D shows the image acquired using Oxymap Tx ehf. for comparison. Scale bar represents 300 μm in the retina.

The S values of these vessels are similar to the values obtained by dual-wavelength imaging of the same volunteer (Fig. 5.9) and oxygen saturation maps obtained with Oxymap Tx e.h.f. The errors on the fitted parameters were calculated from the diagonals of the covariance matrix [51]. From the fitted values of $\langle L_{eff} \rangle$, the relationship between $\langle L_{eff} \rangle$ and D_{ves} for these vessels ($D_{ves} \geq 70 \mu\text{m}$) could be established, and this relationship is plotted in Figure 5.13. The relation between $\langle L_{eff} \rangle$ and D_{ves} was found to be fitted well by a linear function, $\langle L_{eff} \rangle [\mu\text{m}] = (0.46 \cdot D_{ves} + 5.2) \pm 6.0 [\mu\text{m}]$ where $\langle L_{eff} \rangle$ and D_{ves} are given in micrometres. From this relationship we conclude that our sub-diffuse SLO imaging scheme, where a small illumination spot is used in combination with a large collection aperture, works in a light transport regime between a fundus camera (where $\langle L_{eff} \rangle = D_{ves}$) and a truly confocal SLO (where $\langle L_{eff} \rangle = \langle L_{bs} \rangle$ with $\langle L_{bs} \rangle$ the backscatter path length which is not expected to have a linear dependence on D_{ves}). We expect that the exact relation between $\langle L_{eff} \rangle$ and D_{ves} depends on the details of the measurement geometry, and will, for example, be different for different DCF cladding sizes or, equivalently, for different confocal aperture sizes. Furthermore, we have here in our fits assumed $\langle L_{eff} \rangle$ to be wavelength independent, whereas it is expected that $\langle L_{eff} \rangle$ depends on the scattering and absorption coefficients of blood and is therefore in reality wavelength dependent. This is a topic for future investigations.

One notable advantage of the wavelength sweep using the SLO is the availability of the spectral properties of the entire retina for multiple wavelengths. This will in the future permit expansion of the diagnostic capabilities of an SLO by providing spectral fingerprints of additional chromophores such as carotenoids. However, the imaging speed of the wavelength sweep should be dramatically improved before the clinical implementation of wavelength sweeping would become feasible.

5.4 Conclusion

In conclusion, we have demonstrated *in vivo* human retinal imaging with a novel SLO based on a supercontinuum source. The RIN noise of the illumination source has been addressed by implementing balanced detection. The balanced detection increased the SNR, and therefore improved the image quality and accuracy of oximetry calculations. The implementation of an achromatizing lens reduced the effect of chromatic aberrations introduced by the human eye, although this did not have a large effect on saturation estimation. The use of a double clad fibre with large inner cladding provided the best trade-off between image contrast and SNR. This allowed for high-resolution *in vivo* visualization of the oxygenation of retinal

blood vessels in healthy volunteers. The oxygen saturation of the larger vessels of the retinas of two human volunteers were in agreement with the Oxymap derived saturations; in addition, our SLO system was able to provide oxygen saturation in much smaller vessels. The saturation measured in 3 different imaging sessions of the same volunteer (8 minutes apart) demonstrated the reproducibility of our measurements. Finally, by performing a wavelength sweep between 485 and 608 nm we determined an approximately linear relationship between the effective path length of photons through the blood vessels and vessel diameter for our SLO geometry that employs a DCF with a large inner cladding. It is expected that our SLO will be a valuable tool to study the effect of degenerative retinal diseases on the oxygenation in the retinal microvasculature.

References

- [1] N. D. Wangsa-wirawan and R. Linsenmeier, "Retinal Oxygen," *Arch Ophthalmol.* **121**, 547557 (2003).
- [2] T. Bek, E. Stefansson and S. H. Hardarson, Retinal oxygen saturation is an independent contributor to the severity of retinopathy in diabetic patients, *Br. J. Ophthalmol.*, 103 (8), 1167 1172 (2018).
- [3] E. D. Cole, E. A. Novais, R. N. Louzada, and N. K. Waheed, "Contemporary retinal imaging techniques in diabetic retinopathy: a review," *Clin. Exp. Ophthalmol.* **44**, 289299 (2016).
- [4] R. Klein, B. E. K. Klein, M. W. Neider, L. D. Hubbard, S. M. Meuer, and R. J. Brothers, "Diabetic Retinopathy as Detected Using Ophthalmoscopy, a Nonmyciariatic Camera and a Standard Fundus Camera," *Ophthalmology* **92**, 485491 (1985).
- [5] G. Michelson, M. Scibor, and D. Schweitzer, "Intravascular oxygen saturation in retinal vessels in glaucoma," *Invest. Ophthalmol. Vis. Sci.* **43**, U445U445 (2002).
- [6] A. Geirsdottir, S. H. Hardarson, O. B. Olafsdottir, and E. Stefansson, "Retinal oxygen metabolism in exudative age-related macular degeneration," *Acta Ophthalmol.* **92**, 2733 (2014).
- [7] O. B. Olafsdottir, S. H. Hardarson, M. S. Gottfredsdottir, A. Harris, and E. Stefansson, "Retinal oximetry in primary open-angle glaucoma," *Investig. Ophthalmol. Vis. Sci.* **52**, 64096413 (2011).
- [8] E. Nitta, K. Hirooka, T. Shimazaki, S. Sato, K. Ukegawa, Y. Nakano, and A. Tsujikawa, "Retinal oxygen saturation before and after glaucoma surgery," *Acta Ophthalmol.* 20152018 (2016).
- [9] S. Rilver, T. L. Torp, and J. Grauslund, "Retinal oximetry in patients with ischaemic retinal diseases," *Acta Ophthalmol.* **95**, 119127 (2017).
- [10] A. B.Einarsdottir et al., Retinal oximetry imaging in Alzheimers disease, *J. Alzheimers Dis.*, **49** (1), 79 83 (2015).
- [11] N. J. Hart, Y. Koronyo, K. L. Black, and M. Koronyo-Hamaoui, "Ocular indicators of Alzheimer's: exploring disease in the retina," *Acta Neuropathol.* **132**, 767787 (2016).
- [12] A. B. Einarsdottir, O. B. Olafsdottir, H. Hjaltason, and S. H. Hardarson, "Retinal oximetry is affected in multiple sclerosis," *Acta Ophthalmol.* **96**, 528530 (2018).
- [13] T. Shiba, K. Maruo, and T. Akahoshi, "Development of a multi-field fundus photographing system using a non-mydratiac camera for diabetic retinopathy," *Diabetes Res. Clin. Pract.* **45**, 18 (1999).
- [14] E. DeHoog and J. Schwiegerling, "Optimal parameters for retinal illumination and imaging in fundus cameras.," *Appl. Opt.* **47**, 67696777 (2008).
- [15] A. Geirsdottir, S. H. Hardarson, O. B. Olafsdottir, and E. Stefansson, "Retinal oxygen metabolism in exudative age-related macular degeneration," *Acta Ophthalmol.* **92**, 2733 (2014).
- [16] J. C. Ramella-Roman, S. a Mathews, H. Kandimalla, A. Nabili, D. D. Duncan, S. a DAnna, S. M. Shah, and Q. D. Nguyen, "Measurement of oxygen saturation in the retina with a spectroscopic sensitive multi aperture camera.," *Opt. Express* **16**, 61706182 (2008).
- [17] D. J. Mordant, I. Al-Abboud, G. Muyo, A. Gorman, A. Sallam, P. Ritchie, A. R. Harvey, and A. I. McNaught, "Spectral imaging of the retina," *Eye* **25**, 309320 (2011).

- [18] B. Khoobehi, J. M. Beach, and H. Kawano, "Hyperspectral Imaging for Measurement of Oxygen Saturation in the Optic Nerve Head," *Invest. Ophthalmol. Vis. Sci.* **45**, 146472 (2004).
- [19] W. R. Johnson, D. W. Wilson, W. Fink, M. Humayun, and G. Bearman, "Snapshot hyperspectral imaging in ophthalmology," *J. Biomed. Opt.* **12**, 014036 (2014).
- [20] R. A. Ashman, F. Reinholz, and R. H. Eikelboom, "Oximetry with a multiple wavelength SLO," *Int. Ophthalmol.* **23**, 343346 (2001).
- [21] H. Li, J. Lu, G. Shi, and Y. Zhang, "Measurement of oxygen saturation in small retinal vessels with adaptive optics confocal scanning laser ophthalmoscope," *J. Biomed. Opt.* **16**, 110504 (2011).
- [22] S. P. Chong, M. Bernucci, H. Radhakrishnan, and V. J. Srinivasan, "Structural and functional human retinal imaging with a fiber-based visible light OCT ophthalmoscope," *Biomed. Opt. Express* **8**, 323 (2017).
- [23] L. E. MacKenzie, T. R. Choudhary, A. I. McNaught, and A. R. Harvey, "In vivo oximetry of human bulbar conjunctival and episcleral microvasculature using snapshot multispectral imaging," *Exp. Eye Res.* **149**, 4858 (2016).
- [24] J. P. Campbell, M. Zhang, T. S. Hwang, S. T. Bailey, D. J. Wilson, Y. Jia, and D. Huang, "Detailed Vascular Anatomy of the Human Retina by Projection-Resolved Optical Coherence Tomography Angiography," *Sci. Rep.* **7**, 111 (2017).
- [25] S. Pi, A. Camino, X. Wei, J. Simonett, W. Cepurna, D. Huang, J. C. Morrison, and Y. Jia, "Rodent retinal circulation organization and oxygen metabolism revealed by visible-light optical coherence tomography," *Biomed. Opt. Express* **9**, 58515862 (2018).
- [26] M. Damodaran, A. Amelink, and J. F. de Boer, "Optimal wavelengths for subdiffuse scanning laser oximetry of the human retina," *J. Biomed. Opt.* **23**, 1 (2018).
- [27] A. Sassaroli and S. Fantini, "Comment on the modified Beer-Lambert law for scattering media," *Phys. Med. Biol.* **49**, (2004).
- [28] L. Kocsis, P. Herman, and A. Eke, "The modified Beer-Lambert law revisited," *Phys. Med. Biol.* **51**, (2006).
- [29] N. Bosschaart, G. J. Edelman, M. C. G. Aalders, T. G. van Leeuwen, and D. J. Faber, "A literature review and novel theoretical approach on the optical properties of whole blood," *Lasers Med. Sci.* **29**, 453479 (2014).
- [30] N. Rajaram, A. Gopal, X. Zhang, and J. W. Tunnell, "Experimental validation of the effects of microvasculature pigment packaging on in vivo diffuse reflectance spectroscopy," *Lasers Surg. Med.* **42**, 680688 (2010).
- [31] J. C. Finlay and T. H. Foster, "Effect of pigment packaging on diffuse reflectance spectroscopy of samples containing red blood cells," *Opt. Lett.* **29**, 965967 (2004).
- [32] D. Schweitzer, M. Hammer, J. Kraft, E. Thamm, E. Königsdörffer, and J. Strobel, "In vivo measurement of the oxygen saturation of retinal vessels in healthy volunteers," *IEEE Trans. Biomed. Eng.* **46**, 14541465 (1999).
- [33] "International Electrotechnical Commission, Safety of Laser Products Part 1: Equipment Classification and Requirements", (Geneva, Switzerland), IEC-60825-1 (2014),
- [34] APD410x Operation Manual, Thorlabs GmbH, Germany (2015).
- [35] S. Lemire-Renaud, M. Rivard, M. Strupler, D. Morneau, F. Verpillat, X. Daxhelet, N. Godbout, and C. Boudoux, "Double-clad fiber coupler for endoscopy," *Opt. Express* **18**, 975564 (2010).
- [36] E. De Montigny, W.-J. Madore, O. Ouellette, G. Bernard, M. Leduc, M. Strupler, C. Boudoux, and N. Godbout, "Double-clad fiber coupler for partially coherent detection," *Opt. Express* **23**, 90409051 (2015).
- [37] W. J. Donnelly and A. Roorda, "Optimal pupil size in the human eye for axial resolution," *J. Opt. Soc. Am. A. Opt. Image Sci. Vis.* **20**, 20102015 (2003).

- [38] M. Vinas, C. Dorronsoro, D. Cortes, D. Pascual, and S. Marcos, "Longitudinal chromatic aberration of the human eye in the visible and near infrared from wavefront sensing , double-pass and psychophysics," *Biomed. Opt. Express* **23**, 513522 (2015).
- [39] I. B. Gonzalo, R. D. Engelsholm, and O. Bang, "Noise study of all-normal dispersion supercontinuum sources for potential application in optical coherence tomography," *Prog. Biomed. Opt. Imaging - Proc. SPIE* 10591, (2018).
- [40] G. McConnell, "Noise analysis of a white-light supercontinuum light source for multiple wavelength confocal laser scanning fluorescence microscopy," *J. Phys. D: Appl. Phys.* **38**, 26202624 (2005).
- [41] J. M. Dudley, S. Coen, K. L. Corwin, N. R. Newbury, B. R. Washburn, S. A. Diddams, and R. S. Windeier, "Fundamental noise limitations on supercontinuum generation in microstructure fiber," *Phys. Rev. Lett.* **90**, 113904 (2003).
- [42] D. G. Lowe, "Distinctive Image Features from Scale-Invariant Keypoints," *Int. J. Comput. Vis.* **50**, 91110 (2004).
- [43] V. Davidoiu, L. Hadjilucas, I. Teh, N. P. Smith, J. E. Schneider, and J. Lee, "Evaluation of noise removal algorithms for imaging and reconstruction of vascular networks using micro-CT," *Biomed. Phys. Eng. Express* **2**, 45015 (2016).
- [44] K. Zuiderveld, "Contrast Limited Adaptive Histogram Equalization," in *Graphics Gems IV*, P. S. Heckbert, ed. (Academic Press Professional, Inc., 1994), pp. 474485.
- [45] P. Bankhead, C. N. Scholfield, J. G. McGeown, and T. M. Curtis, "Fast retinal vessel detection and measurement using wavelets and edge location refinement," *PLoS One* **7**, 112 (2012).
- [46] D. A. Atchison and G. Smith, *Optics of the Human Eye*, Butterworth-Heinemann, Oxford (2000).
- [47] E. J. Fernández, A. Unterhuber, B. Povaay, and B. Hermann, "Chromatic aberration correction of the human eye for retinal imaging in the near infrared," **14**, 16731680 (2006).
- [48] R. J. Zawadzki, B. Cense, Y. Zhang, S. S. Choi, D. T. Miller, and J. S. Werner, "Ultrahigh-resolution optical coherence tomography with monochromatic and chromatic aberration correction," *Opt. Express* **16**, 17341746 (2008).
- [49] S. P. Chong, T. Zhang, A. Kho, M. T. Bernucci, A. Dubra, and V. J. Srinivasan, "Ultrahigh resolution retinal imaging by visible light OCT with longitudinal achromatization," *Biomed. Opt. Express* **9**, 1477 (2018).
- [50] F. LaRocca, D. Nankivil, S. Farsiu, and J. A. Izatt, "True color scanning laser ophthalmoscopy and optical coherence tomography handheld probe," *Biomed. Opt. Express* **5**, 3204 (2014).
- [51] A. Amelink, D. J. Robinson, and H. J. C. M. Sterenborg, "Confidence intervals on fit parameters derived from optical reflectance spectroscopy measurements," *J. Biomed. Opt.* **13**, 114 (2008).

